

ARTICLE OPEN



Indian Ocean Dipole and ENSO's mechanistic importance in modulating the ensuing-summer precipitation over Eastern China

Yue Zhang ^{1,2}, Wen Zhou ^{1,2}✉, Xin Wang³, Sheng Chen³, Jiepeng Chen³ and Shanshan Li⁴

Eastern China was extremely wet in summer 2020, which is found to be related to the potential delayed effects of the Indian Ocean Dipole (IOD). Additional knowledge is warranted to improve our understanding of detailed mechanisms of such an effect. In this study, we compared physical processes associated with delayed effects of the IOD and El Niño–Southern Oscillation (ENSO) on summer precipitation. Partial correlation and composite analysis reveal that ENSO modulates precipitation mainly over the Yangtze River Valley, whereas IOD benefits precipitation farther north. Both IOD and ENSO can stimulate anticyclonic circulation over the western North Pacific (WNP) in the ensuing summer but with different spatial distributions related to the different sea surface temperature (SST) evolution processes. IOD is similarly followed by warming signals in the Indian Ocean, known as the “capacitor” effect, but the location is closer to Australia than that associated with ENSO. IOD also stimulates significant SST cooling anomalies over the equatorial Pacific during the ensuing summer, jointly contributing to the anomalous anticyclone over WNP. Numerical experiments confirm that combined effects of the Indian Ocean “capacitor” and equatorial Pacific cooling can generate an anomalous anticyclone with wider distribution in the meridional direction over WNP.

npj Climate and Atmospheric Science (2022)5:48; <https://doi.org/10.1038/s41612-022-00271-5>

INTRODUCTION

The Indian Ocean Dipole (IOD) is an intrinsic air–ocean coupling mode in the Indian Ocean (IO)^{1,2}, which is a counterpart to the climate-driving El Niño–Southern Oscillation (ENSO) in the equatorial East Pacific. Conventionally, summer monsoonal precipitation variation over East Asia is modulated largely by ENSO events^{3–9}. IOD, however, has also been found to be able to significantly influence summer precipitation over East Asia^{10–13} during its developing stage. Since the severe floods in eastern China during the summer of 2020 have been linked to the influence of the extreme positive IOD the preceding year^{14–18}—mainly through an Indian Ocean warming “capacitor” effect in the following spring and summer—positive IOD can trigger a westward-propagating oceanic downwelling Rossby wave that reaches the southwestern Indian Ocean in spring. This extreme event suggests the importance of considering the delayed effects of IOD on the ensuing summer.

The delayed effects of the preceding IOD on the following summer climate have previously been underestimated, mainly due to the complex and interactive relationship between IOD and ENSO. IOD usually develops in summer and peaks in autumn, a season leading the peak of El Niño, then quickly declines in winter^{1,2,19,20}; meanwhile, ENSO tends to develop over the eastern equatorial Pacific but peaks in winter of the same year²¹. During the life span of these two climate modes, they interact so that each affects the intensity, lifetime, and pattern of the other mode^{22–28}. In terms of the relationship between summer monsoonal precipitation and ENSO, the most noteworthy responses occur mainly during the decaying phase of ENSO the following year^{29–34}, which can be considered a delayed effect of ENSO. Similarly, the delayed effect of IOD also refers to the

response of summer precipitation the following year, but few studies have addressed this phenomenon^{35–37}. Generally, associated with a preceding positive IOD, summer precipitation is expected to be enhanced around the Yangtze River region^{35–37}. Nonetheless, considering the important modulations of ENSO on precipitation around the Yangtze River^{34,38–40}, it is worth clarifying the similarities and dissimilarities associated with summer precipitation responses to IOD and ENSO.

Regarding the devastating floods in eastern China during the summer of 2020, many studies have emphasized that warming in the Indian Ocean (IO)^{14–18} was responsible for the abnormal precipitation, which was in turn associated with the preceding IOD^{14,15}. Therefore, a promising mechanism has been proposed to explain this complex cross-seasonal relationship, which is the IO “capacitor” effect¹⁴. Associated with a positive IOD, warming anomalies may occur in the southwestern IO that can act like a “capacitor” and sustain the impacts of IOD on the ensuing seasons. The IO “capacitor” is also one of the essential theories for maintaining the delayed impacts of ENSO^{9,41}. Hence, the present study also addresses the question of the difference between the “capacitor” effect corresponding to IOD and ENSO, and clarifies whether the “capacitor” effect of all IOD cases is as prominent as that in the summer of 2020.

Therefore, this study is aimed primarily at better understanding the delayed effects of IOD by differentiating the impacts and mechanisms of IOD from those of ENSO based on data during 1979–2021. The impacts of IOD and ENSO on the ensuing summer precipitation are first compared, with an additional focus on the contribution of water vapor transport. Mechanisms associated with these two climate modes are examined by the seasonal evolution of large-scale circulation and sea surface temperature

¹Department of Atmospheric and Oceanic Sciences and Institute of Atmospheric Sciences, Fudan University, Shanghai, China. ²Guy Carpenter Asia-Pacific Climate Impact Centre, School of Energy and Environment, City University of Hong Kong, Hong Kong, China. ³State Key Laboratory of Tropical Oceanography, South China Sea Institute of Oceanology, Chinese Academy of Sciences, Guangzhou, China. ⁴Guangdong Meteorological Observatory, Guangzhou, China. ✉email: wen_zhou@fudan.edu.cn

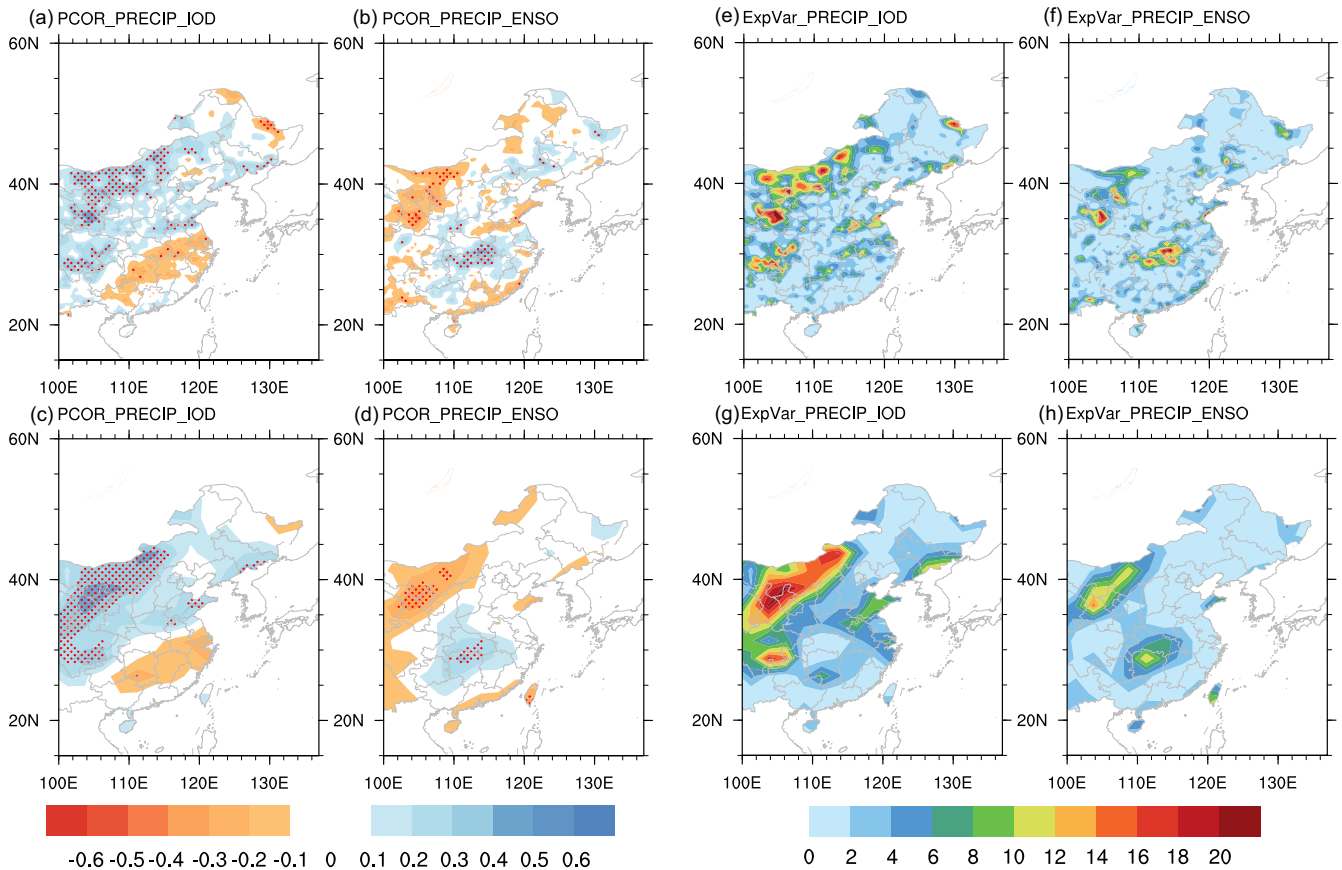


Fig. 1 Precipitation patterns associated with the preceding IOD and ENSO. Partial correlations of precipitation during the ensuing summer with the DMI of the preceding autumn after removing the linear relationship with Niño 3.4 of winter based on **a** station precipitation data, and **b** GPCP data during 1979–2021. **c** and **d** as in **a** and **b**, but with Niño 3.4 of winter after deducing the linear relationship with the DMI of the preceding autumn. Variance fraction of summer precipitation (%) accounted for by **e** and **f** the DMI in autumn and **g**, **h** Niño 3.4 in winter based on **e**, **g** station data, and **f**, **h** GPCP data. Dotted areas in **a–d** represent statistical significance at the 95% confidence level.

(SST). Important forcing effects of the associated SST patterns in the ensuing summer are further investigated with a 5-layer anomalous atmospheric general circulation model (AGCM).

RESULTS

Different ensuing summer precipitation patterns associated with IOD and ENSO

The different summer precipitation patterns associated with IOD and ENSO are first examined by partial correlation analysis, which aims to separate the influence of these two modes by eliminating the linear relationship between IOD and ENSO based on station observations as well as the reanalysis precipitation dataset during 1979–2021. After deducing the linear relationship with ENSO, Global Precipitation Climatology Project (GPCP) and station data both indicate that IOD benefits mainly precipitation over the region north of the Yangtze River, while it also tends to induce drier conditions over South China (Fig. 1a, c). The response of precipitation to the preceding ENSO is primarily excessive precipitation around the Yangtze River Valley, which is quite consistent with previous results (Fig. 1b, d,^{3,4,42,43}). These patterns confirm that both IOD and ENSO have the potential to boost precipitation in the following summer, but with different centers of maximum influence. Although the impacts of ENSO can be seen directly in flooding in the Yangtze River Valley, IOD can also substantially influence precipitation over the upper reaches of the Yangtze River Valley as well as over other main rivers in eastern China, such as the Huaihe River and Yellow River.

The explained variance can also be calculated to evaluate the relative contribution of these two climate modes to precipitation variation, with results shown in Fig. 1e–h. This shows that IOD can contribute up to 20% of the precipitation variation for parts of northern China such as Inner Mongolia, whereas ENSO contributes to precipitation variation mainly around the Yangtze River and parts of northwestern China. Statistically, the above investigation indicates that for the following summer precipitation, IOD plays as important a role as ENSO in modulating summer precipitation, and IOD also deserves attention to help improve the seasonal predictability of summer precipitation in eastern China.

Large-scale background and water vapor transport variation associated with the preceding IOD and ENSO

In order to further examine the underlying mechanisms by which IOD and ENSO lead to summer climate anomalies, composite analysis is conducted as well. Using the dipole mode index (DMI;¹) and the Niño 3.4 index to characterize the interannual variation of IOD and ENSO events (Supplementary Fig. 1), and based on 0.5 standard deviation of these indices, positive and negative cases of IOD and ENSO can be identified, as documented in Table 1. Based on different combinations of IOD and ENSO events, composite analysis can be employed accordingly to investigate how precipitation varies with only the preceding IOD or only the preceding ENSO, compared to when both phenomena occur.

The composite difference based on positive and negative cases generally reproduces the symmetric impacts of the climate mode, shown as anomalous signals related to a positive event.

Therefore, Fig. 2a illustrates the atmospheric responses in summer associated with the preceding positive IOD without El Niño. Positive anomalies of geopotential height are dominant around the western North Pacific (WNP) and extend into the mid-latitudes, which tends to enhance the subtropical high, thus influencing convection and water vapor transport over East Asia. Water vapor flux over the WNP is characterized as an anticyclonic circulation

Table 1. Years of the different combinations of ENSO and IOD events.

IOD and ENSO combination	Years
pIOD without El Niño	2011, 2012, 2019
nIOD without La Niña	1979, 1980, 1981, 1989, 1990, 1992, 1996, 2001, 2016
El Niño without pIOD	1979, 1987, 2004, 2009
La Niña without nIOD	1999, 2000, 2007, 2008, 2011, 2013, 2017
pIOD + El Niño	1982, 1986, 1991, 1994, 1997, 2002, 2006, 2015, 2018
nIOD + La Niña	1984, 1988, 1995, 1998, 2005, 2010

pIOD means positive IOD events; nIOD means negative IOD events. Years listed denote the years when IOD/ENSO develops.

pattern, such that moist air from the tropics is transported northward along its western flank all the way to 40°N (Fig. 2d). In addition, eastward water vapor transport is also salient over land, indicating that water vapor provided by westerly jets also increases. Under the influence of the anomalous large-scale circulation and water vapor flux, the composite precipitation is also plotted to demonstrate the precipitation anomalies in association with the preceding IOD. Positive precipitation anomalies dominate again in the region north of the Yangtze River, and the most significant responses appear in the more northern areas (Fig. 2g), creating a dipole pattern with opposite precipitation anomalies south and north of the Yangtze River.

The atmospheric fields are further examined to reveal the differences and similarities in the responses associated with ENSO (Fig. 2b, e, h). In the mid-troposphere, significant increasing geopotential height is obvious over the WNP following a El Niño event. An enhanced subtropical high denoted by anticyclonic circulations around the WNP can also be observed in the lower troposphere (Supplementary Fig. 2b). Driven by the anomalous anticyclone, the water vapor transport associated with ENSO-only forcing also shows an anticyclonic pattern, conveying moist air from the tropical western Pacific into eastern China and condensing mainly in the Yangtze River Valley. Hence, in the summer after El Niño without IOD, precipitation is evidently

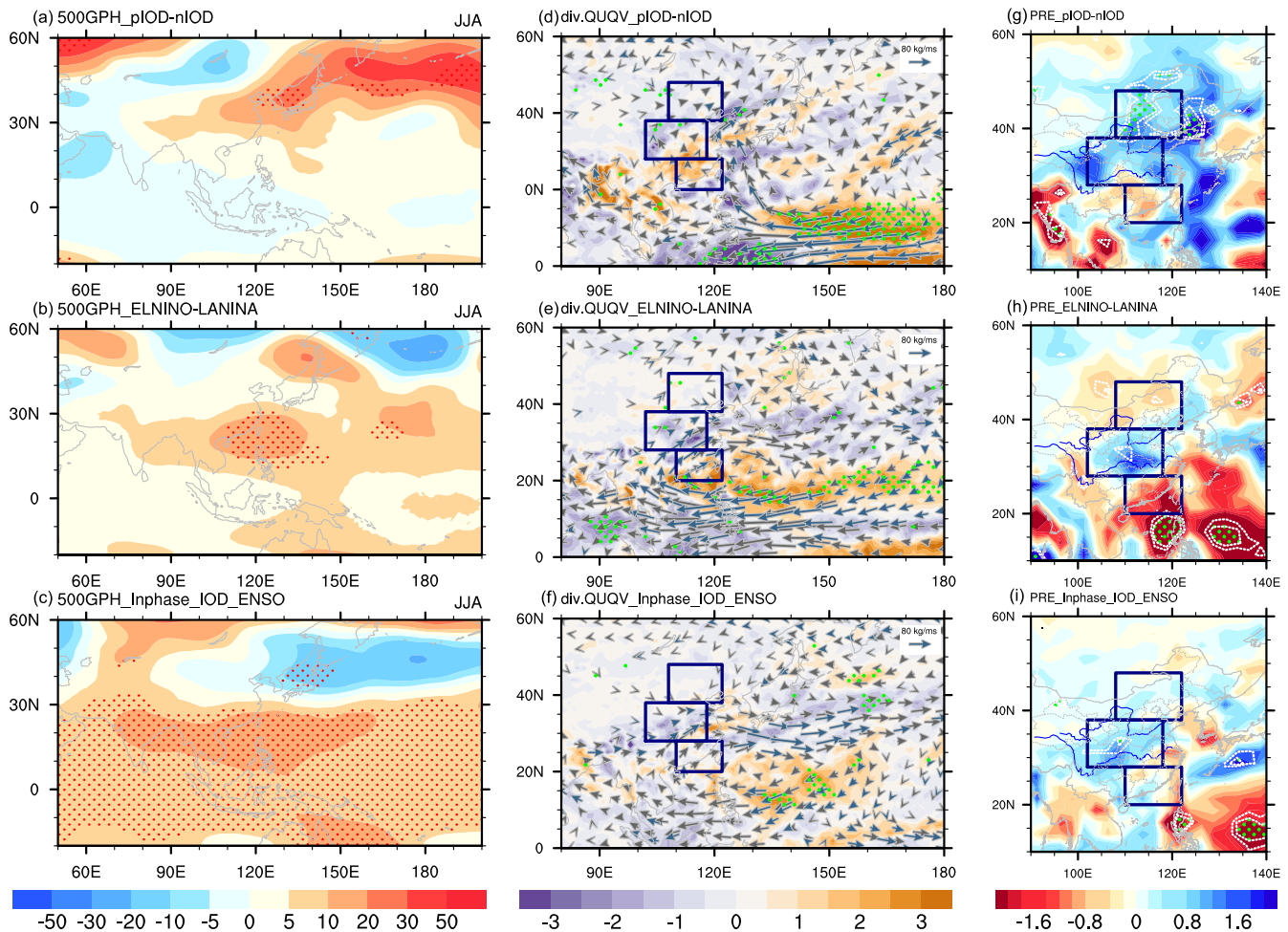


Fig. 2 Composites of atmospheric fields associated with the preceding IOD and ENSO. Composite difference of **a–c** geopotential height (shading; $\text{m}^2 \text{s}^{-2}$) at 500 hPa during the ensuing summer based on the years when **a** only IOD occurs, **b** only El Niño occurs, and **c** IOD and ENSO occur together. **d–f** as in **a–c** but for vertically integrated water vapor flux (vectors, $\text{kg m}^{-1} \text{s}^{-1}$; showing only values greater than $10 \text{ kg m}^{-1} \text{s}^{-1}$) and its convergence (shading; kg m^{-2}). **g–i** as in **a–c** but for precipitation (mm day^{-1}). Dotted areas mean that signals are statistically significant at the 95% confidence level. Blue vectors in **d–f** indicate that the vertically integrated water vapor flux exceeds the 95% confidence level. Boxes in **d–i** indicate the key regions for water vapour budget analysis.

enhanced over the middle reaches of the Yellow River Valley, while negative precipitation signals occur over the tropics and eastern Inner Mongolia (Fig. 2h), leading to a tripole-like pattern, which also agrees with results of previous studies on the influence of ENSO on the decaying summer precipitation^{6,42}. The differences in the precipitation anomalies associated with IOD-only and ENSO-only forcings may be related to the different characteristics of the anomalous anticyclone circulation pattern as well as geopotential height distribution. During the summer following IOD alone, the meridional range of the anomalous anticyclone is within 20°–40°N (Fig. 2d), while the meridional range of the anomalous anticyclone associated with ENSO forcing alone is relatively narrower, covering 20°–30°N (Fig. 2e). As a result, the most salient increase in precipitation occurs farther north in the summer following IOD.

During the summers of co-occurring IOD and ENSO, positive geopotential anomalies are evident all over the tropics (Fig. 2c), suggesting that the heat source related to the positive IOD and El Niño forcings is greatly amplified due to their interaction^{22,26,27,44}. For example, Luo et al. revealed that a positive IOD can enhance the strength of El Niño and facilitate its onset; in turn, El Niño can also enhance IOD and improve its predictability via the atmospheric Walker circulation. Meanwhile, an enhanced and west-shifted subtropical high is also noticeable (Fig. 2c, f), with a pattern quite similar to that during ENSO-only years, indicating the more dominant role of ENSO in modulating the ensuing summer precipitation. However, for precipitation in northern China, the impacts of IOD seem to be opposite to those of ENSO, so the impacts of these two climate modes cancel each other, leading to an insignificant pattern. The increased precipitation associated with IOD in northern China can be attributed to the greater amount of moisture transported by westerly jets, which can be observed in both summers preceded by IOD with and without ENSO (Fig. 2d, f). During the summer following IOD along with ENSO, the resulting precipitation pattern is more likely to have a dipole-like pattern, with opposite responses south and north of the Yangtze River (Fig. 2i).

Regional water vapor budget analysis

Based on the anomalous poles of the different precipitation patterns associated with the different combinations of IOD and ENSO, highlighting the key areas of eastern China, water vapor budget analysis is conducted to reveal the roles of the preceding IOD and ENSO in modulating precipitation by influencing moisture transport, with results documented in Table 2. For convenience, three key areas, based mainly on the tripole-like precipitation pattern associated with ENSO-only forcing, are defined as South China (SC; 20°–28°N, 110°–122°E), the basin between the Yangtze and Yellow Rivers (YY; 28°–38°N, 102°–118°E), and northern China (NC; 38°–48°N, 108°–122°E). First, the total regional water vapor budget can largely account for the precipitation variability in these regions, with high explained variance of 90.95% for SC, 64.55% for YY, and 63.46% for NC. Based on a significance test, it is noticeable that precipitation variation in YY is more sensitive to the external forcings of IOD and ENSO, which may be to some extent because this region also has large interannual variation (Supplementary Fig. 3a).

For SC, significant contributions are elucidated in water vapor transport only through the western and eastern boundaries, and the relatively important factor in modulating the zonal water vapor transport is ENSO. Associated with El Niño, water vapor inflow through the western boundary increases but water vapor outflow through the eastern boundary also increases (Supplementary Fig. 4c), so eventually the effects of ENSO on the moisture budget are insignificant. For YY, both IOD and ENSO can significantly modulate water vapor transport. IOD can contribute a lot to the water vapor budget by influencing the water vapor flow through three of the lateral boundaries, except

Table 2. Water vapor budget analysis based on key regions (fraction of explained variance, %).

	Precip.	Budget	Western	Southern	Eastern	Northern
South China (SC)						
DMI	2.57	4.97	6.91*	2.33	3.75	6.79
NINO34	6.35	8.81	14.17#	3.49	11.27#	8.43
DMI+NINO34	6.39	9.25	14.53#	3.81	11.27*	9.78
Yangtze-Yellow basin (YY)						
DMI	32.30#	14.16#	14.97#	17.93#	12.72#	0.06
NINO34	11.99#	5.08	15.33#	18.18#	22.62#	2.48
DMI+NINO34	32.38#	14.18#	19.32#	23.03#	23.73#	4.37
Northern China (NC)						
DMI	13.20#	5.28	3.22	0.48	0.28	1.59
NINO34	1.71	1.24	0.52	1.07	0.01	1.99
DMI+NINO34	14.04*	5.33	3.35	3.50	0.34	8.28

In each region, the contributions from IOD/ENSO to the precipitation, water vapor budget, and water vapor transport via four lateral boundaries (western, southern, eastern, northern) are documented respectively.

#Statistically significant values at the 95% confidence level.

*Statistically significant values at the 90% confidence level.

the northern one. In contrast, ENSO similarly influences water vapor transport through the western, southern, and eastern boundaries, but contributes only 5% of the total regional moisture budget. This may be related to its more dominant role in enhancing the water vapor outflow through the eastern boundary, which somewhat offsets the positive impacts on the increase in water vapor inflow (Supplementary Fig. 4c). However, although the influence on the moisture budget is limited, ENSO can significantly contribute to precipitation, which indicates that ENSO can also influence precipitation by modulating dynamic factors (such as vertical motion). For NC, only 5% and 1% of the variance in the water vapor budget can be explained by IOD and ENSO, respectively, suggesting a less influential role of tropical forcing effects for the northern region. However, the relatively important effects of IOD can be identified by its significant association with precipitation.

Based on the water vapor analysis, the substantial effects of the preceding IOD on the summer precipitation and moisture supply can be further confirmed. Its role in modulating water vapor transport into the Yangtze River Valley is surely as important as that of ENSO. This implies that the flooding in the Yangtze River basin during the summer of 2020, which was preceded by the most extreme positive IOD in recent decades, is not a specific event. For future climate prediction and disaster mitigation, the delayed effects of IOD should also be emphasized.

Seasonal evolution patterns in the preceding seasons associated with IOD and ENSO

The delayed effects of IOD on the following summer are difficult to understand because IOD has a different lifespan compared to ENSO. It has a relatively shorter lifespan and is believed to disappear quickly during the ensuing winter⁴⁵, so investigations on the mechanisms associated with the delayed effects of IOD are always challenging. However, considering a recent case study of the aftermath of the 2019 IOD, some argue that even in the ensuing summer, the anomalous signals of IOD still remain in the southern IO^{14,15}. The remnant of positive IOD can also act like a

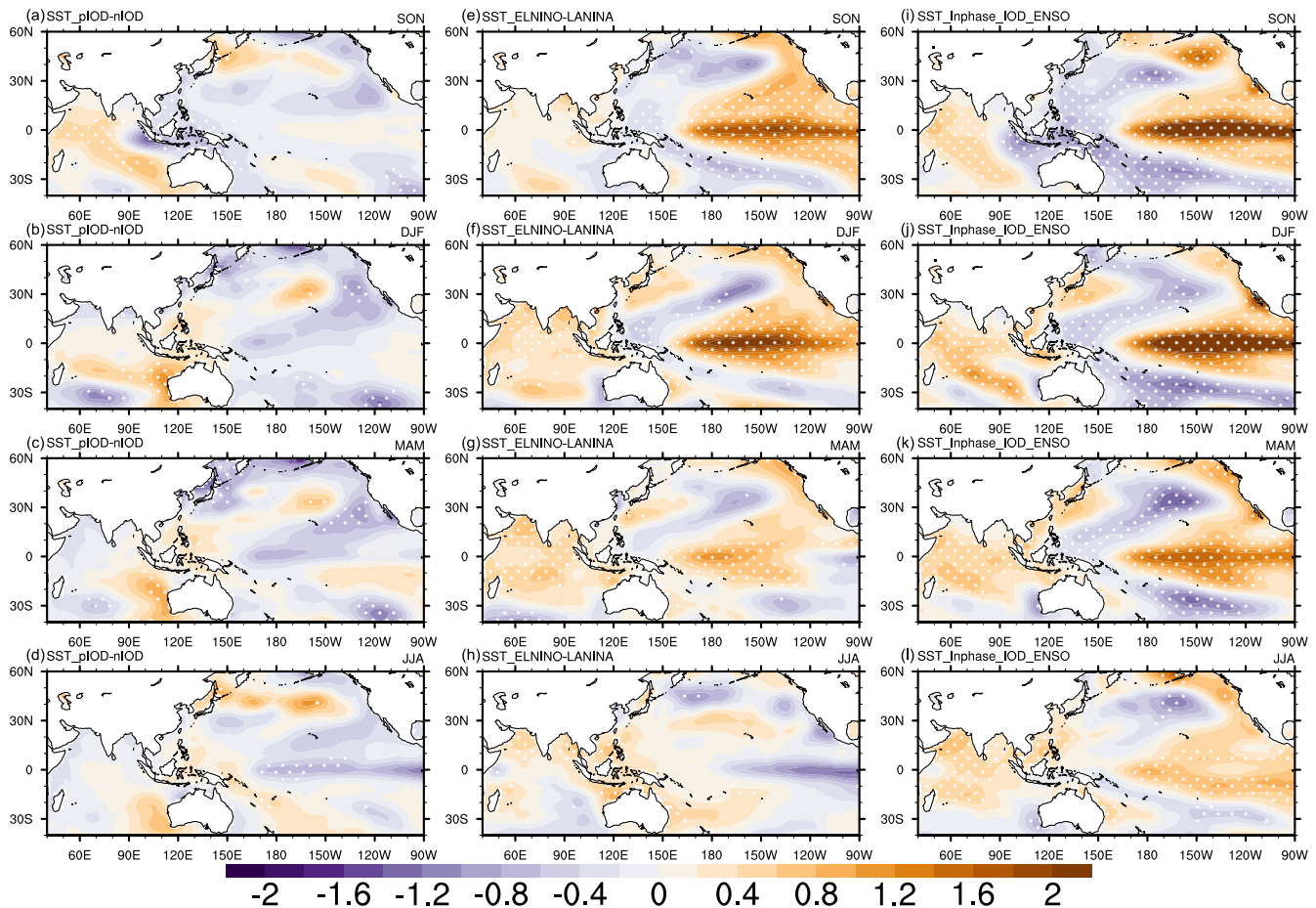


Fig. 3 Seasonal evolution of SST patterns in association with IOD and ENSO. Composite seasonal evolution of SST anomalies (contours, °C) from autumn to the ensuing summer based on the years when **a–d** only IOD occurs, **e–h** only El Niño occurs, and **i–l** IOD and ENSO occur together. Dotted areas have statistical significance at the 95% confidence level.

“capacitor,” with physical processes similar to those of the IO “capacitor” associated with El Niño, thereby inducing an anomalous anticyclone over the WNP. Consequently, the dissimilarities and similarities of the “capacitor” effect associated with IOD and ENSO are worth further comparison and investigation.

The SST evolution associated with IOD and ENSO from autumn to the ensuing summer is examined in Fig. 3 to reveal the spatiotemporal characteristics of different combinations. During autumn when IOD occurs alone without ENSO, the typical SST dipole in the IO can be identified accompanied by an insignificant signal over the equatorial Pacific (Fig. 3a). The western warming pole of SST anomalies extends to the southern IO in a swath from the western equatorial IO to the coast of Australia. This swath slowly propagates and retreats eastward with time, forming a warming center off the coast of Australia during spring. This pattern can be compared with the pattern in the summer of 2020 (Fig. 2 in Zhou et al. 2021), a year with extreme independent positive IOD forcing. There are some similarities: the warming signals are both observed within 0°–30°S of the southern IO. However, the maximum in the composite fields is farther east (Fig. 3c). The significant warming SST off the west coast of Australia is like a Ningaloo Niño pattern, which may be related to a possible linkage between IOD and the Ningaloo Niño, as previous study suggested⁴⁶. The SST anomalies during 2020 are also warm around the coast of Australia, but the magnitudes are inconsiderable (Fig. 2 in Zhou et al. 2021).

During the seasons following El Niño alone, IO basin-wide warming occurs in winter and gradually shrinks and decays in the

ensuing spring and summer (Fig. 3e–h). When IOD and ENSO occur together, the intensity of the SST anomalies over the equatorial eastern Pacific is noticeably greater, requiring more time to oscillate back to the mean stage. Therefore, the warming SST over the equatorial Pacific can still be observed during the ensuing summer (Fig. 3i). Warming SST anomalies over the tropical IO can also last longer than in years with ENSO only and are still significant during summer (Fig. 3l).

Based on the SST patterns in the IO, a preliminary difference in the “capacitor” effect can be revealed. Associated with ENSO, the warming signals in the IO are distributed over both sides of the equator. Generally, the warming signals in the northern IO last longer, which may be because the solar incidence point is in the summer hemisphere and amplifies the warming signal by increasing downward solar radiation⁴⁷. Meanwhile, associated with IOD, the warming signals over the South Indian Ocean (SIO) are also evident, extending from the western equatorial Indian Ocean to the west coast of Australia. The sustenance of the warming anomalies in the SIO during the ensuing seasons may be attributed to the mechanism stated previously^{14,15}: the IOD can induce an anticyclonic circulation pattern over the eastern SIO and consequently lead to Ekman downwelling and a westward-propagating downwelling Rossby wave.

Besides the traits associated with the positive IOD and El Niño phenomena, some significant distinctions exist over the Pacific between years with IOD only and the other two combinations. During seasons following IOD only, significant cooling SST gradually develops over the equatorial Pacific and lasts until the

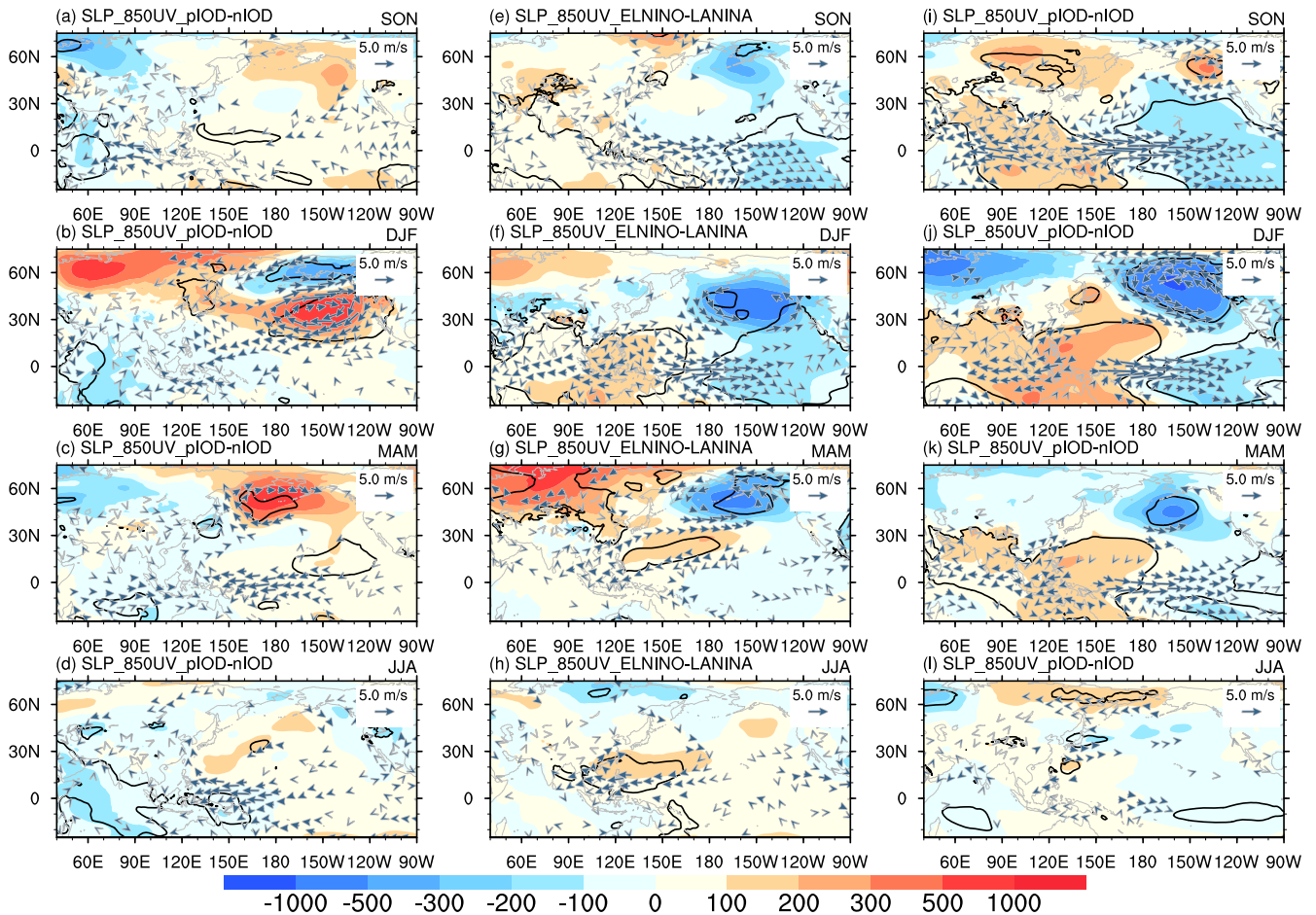


Fig. 4 Seasonal evolution of atmospheric patterns in association with IOD and ENSO. Composite seasonal evolution of horizontal winds (vectors) at 850 hPa and sea surface pressure (shading, Pa) from autumn to the ensuing summer based on the years when **a–d** only IOD occurs, **e–h** only El Niño occurs, and **i–l** IOD and ENSO occur together. Vectors indicate winds that exceed the 95% confidence level. Thick black contours denote sea surface pressure exceeding the 95% confidence level.

ensuing summer, which promotes the development of La Niña. The composite based only on IOD further supports the previous statement that IOD can potentially lead to an out-of-phase ENSO in the subsequent year^{22,48–50}.

Associated with the SST evolution, the circulation in the lower troposphere is also examined to demonstrate the aftermath of these two climate modes. During the years with only IOD forcing, anomalous easterlies are evident over the tropical Pacific after winter (Fig. 4a–c). However, the mechanisms inducing these easterlies during winter should be different from those in the following seasons, due partly to the negative pressure center associated with the warming pole of IOD, and partly to the anomalous anticyclone at higher latitudes. In the following seasons, the anomalous easterlies prevailing over the equatorial Pacific and the westerlies over the equatorial IO should be related to the “capacitor” effect. And based on the theory of local air–sea interaction over the WNP⁴³, the significant cooling SST pattern and the warming SST around the Philippines form a zonal dipole pattern, which could also contribute to the in-situ anomalous anticyclonic circulation (Figs. 3d and 4d).

During the years of ENSO only, the anomalous circulation during autumn and winter is characterized as an anomalous Walker circulation above the Pacific, accompanied by westerlies in the lower troposphere as well as low pressure to the east and high pressure above the Maritime Continent (Fig. 4e, f). This pattern is closely related to the heating of ENSO. Associated with the descending branch of the anomalous Walker circulation, an

abnormal anticyclonic circulation is located over the South China Sea. This anomalous anticyclone persists over the South China Sea and gradually propagates eastward and is sustained in the WNP until the ensuing summer. The evolution of the anomalous anticyclone associated with ENSO during different seasons is consistent with previous studies^{42,51}. The maintenance of the anomalous anticyclone can be attributed to the warming IO (Fig. 3g), known as the IO “capacitor” effect⁹. In the years when IOD and ENSO occur together, the pattern is quite similar to that during the years with ENSO only but with greater intensity. And the anomalous Walker circulation above the Pacific can last until spring (Fig. 4k). During the ensuing summer, only the anomalous anticyclone remnant is maintained over the WNP, influencing the summer circulation (Fig. 4l).

These seasonal evolution patterns clarify the variation in the warming “capacitor” over the IO and in the collaboration of the local air–sea interaction over the WNP between IOD only, ENSO only, and both modes together. Results demonstrate that during IOD-only years, both the IO “capacitor” and local air–sea interaction are in effect, with a significant confidence level; yet the maximum warming SST signals in the IO are farther south and east than during years with ENSO forcing.

Different drivers for the anomalous anticyclone around the western North Pacific

In order to further compare the different driving impacts from the IO and Pacific, a simple AGCM numerical model is employed.

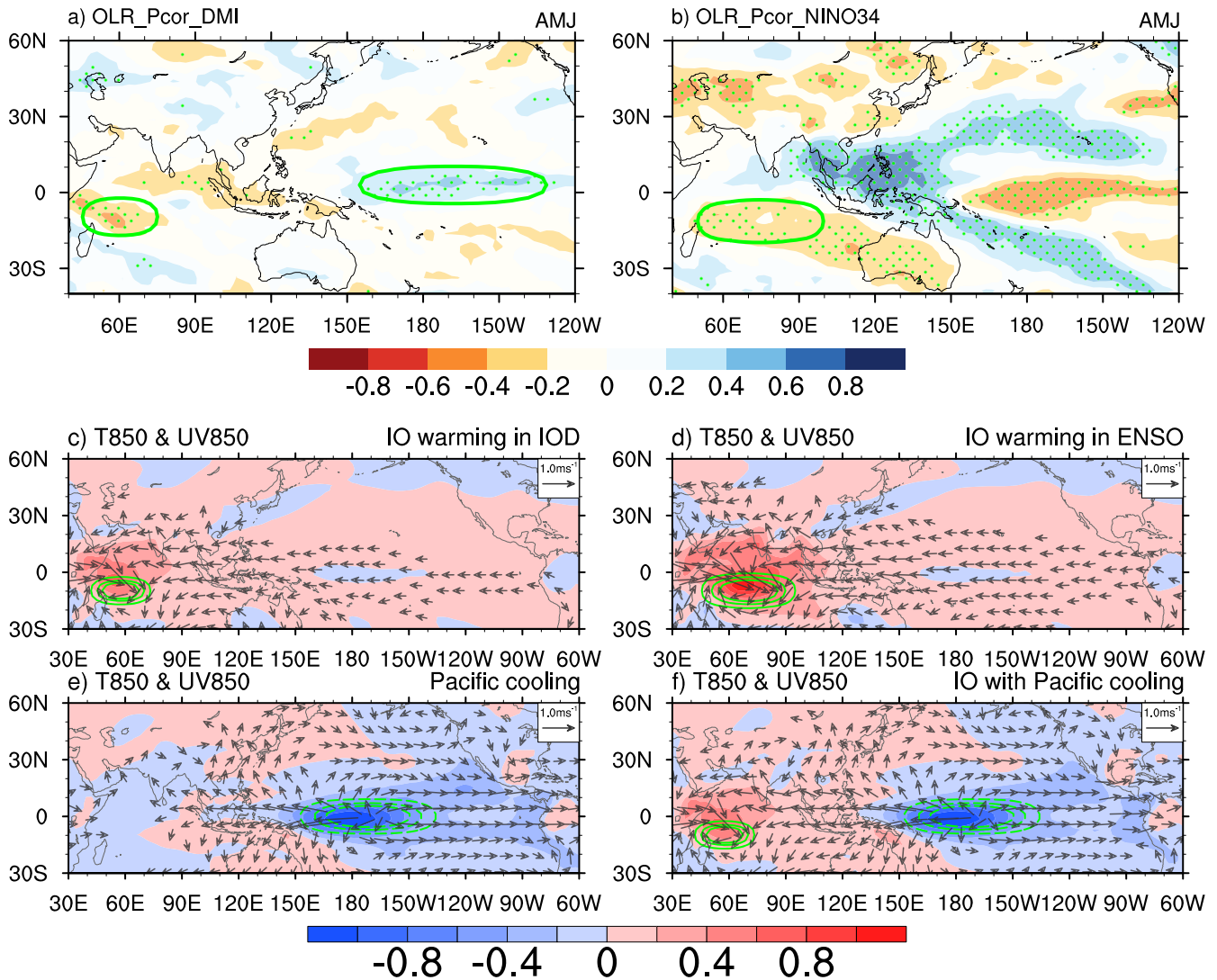


Fig. 5 Heating anomalies and simulation results. **a** Partial correlations of OLR during April–June with the DMI of the preceding autumn after removing the linear relationship with Niño 3.4 of winter. **b** as in **a**, but with Niño 3.4 of winter after deducing the linear relationship with the DMI of the preceding autumn. Air temperature anomalies (shading; K) and horizontal wind anomalies (vectors; showing only magnitudes greater than 0.05 m s^{-1}) at 850 hPa in response to heat anomalies based on the background of climatological mean circulation during April–June. Dotted areas in **a**, **b** have statistical significance at the 95% confidence level. Green contours represent heat patterns, and contours in **c–f** represent heat sources (sinks) at the 0.5 sigma level with an interval of 0.2 K day^{-1} .

The atmospheric heat variation triggered by the IO warming anomalies and Pacific cooling anomalies associated with the preceding positive IOD and El Niño is illustrated by outgoing longwave radiation (OLR). Partial correlation between OLR and the mode indices are shown in Fig. 5a, b, so as to emphasize the direct responses to IOD and ENSO, respectively. A heating source related to the IO “capacitor” effect can be observed mainly in the tropical SIO associated with positive IOD and El Niño, and only the zonal range of heating anomalies associated with El Niño extends more widely (Fig. 5a, b). Corresponding to the SST cooling pattern observed in the composite results (Fig. 3d), a significant heat sink is also evident here (Fig. 5a). Considering that this is closely related to the delayed effects of IOD and also plays a substantial role in the circulation, additional experiments are also designed based on the heat sink center to examine the influence of SST cooling responses in the Pacific. The signals over the Pacific associated with ENSO should otherwise reflect the decay of El Niño itself, so they are not the focus of this study. Apart from partial correlation, composite analysis is also conducted based on tropospheric

temperature and OLR, and they both show heating features similar to the partial correlation results (Supplementary Fig. 5).

The background circulation in the simulation is set up with the climatology circulation during April–June. According to the key anomalous heat pattern reflected by OLR, several numerical experiments are designed. First, we employ the heat source in the IO to represent and compare the “capacitor” effect associated with positive IOD and El Niño, and the prescribed heat anomaly at the 0.5 sigma level is marked by the green contours in Fig. 5c, d. Results show that although the ranges of the heat source vary in association with IOD and ENSO, the primary responses are similar (Fig. 5c, d). The IO “capacitor” can generally induce an asymmetric Gill-type response consisting of anomalous easterlies over the equatorial Pacific and anticyclonic responses in the hemisphere opposite the heating (Fig. 5c, d), which is also consistent with the composite results (Fig. 4d, h, l). Numerical simulations confirm the important role of the IO “capacitor” in producing the anticyclonic responses around the WNP in the ensuing summer of both IOD and ENSO years.

A second pair of experiments are also performed to examine the impacts of SST cooling triggered by the preceding positive IOD with or without the IO heat source. The heat sink over the central equatorial Pacific is prescribed according to the OLR pattern, and the heat anomaly at 0.5 sigma is also shown as contours in Fig. 5e, f. The heat sink can directly trigger an anomalous anticyclone to its west as a Rossby wave response, influencing the East Asian climate (Fig. 5e). Consequently, if the IO “capacitor” and SST cooling work together, the anticyclonic circulation is reinforced and evolves a wider coverage in the meridional direction, which can influence the climate farther north (Fig. 5f). Such simulated patterns prove that these two significant SST forcings associated with the preceding IOD are essential drivers for anomalous summer circulations.

DISCUSSION

Determining the relationship between atmospheric external forcing and precipitation variation is important for the seasonal prediction of precipitation. In this study, the impacts of the preceding IOD and ENSO on summer precipitation over eastern China are examined and compared, with a focus on the distinctive role of IOD. Partial correlation analysis reveals that the key regions of precipitation responses to IOD and ENSO vary: ENSO modulates precipitation mainly over the Yangtze River Valley, whereas IOD benefits precipitation farther north. Composite results also depict a similar tendency of IOD to induce more summer precipitation in regions farther north than ENSO. Both IOD and ENSO can stimulate an anticyclonic circulation response over the WNP in the ensuing summer, but the different spatial distribution of this anomalous anticyclonic circulation leads to different precipitation patterns. Precipitation anomalies associated with ENSO display a tripole-like pattern with an enhanced precipitation center along the Yangtze River. In contrast, if IOD occurs, its impacts in northern China lead to a dipole pattern of precipitation north and south of the Yangtze River. Based on key areas of different precipitation patterns associated with different combinations of conditions for IOD and ENSO, water vapor budget analysis further confirms that precipitation variation around the Yangtze River is more sensitive to the external forcings of IOD and ENSO. Compared to ENSO, IOD is shown to have more substantial impacts on the water vapor budget and precipitation over the two regions (NC and YY) north of the Yangtze River.

Seasonal evolution patterns are plotted to compare the mechanisms associated with the delayed effects of IOD and ENSO on the ensuing summer precipitation. Results illustrate that differences exist in patterns of the warming “capacitor” over the IO. Given that positive IOD can trigger significant SST cooling over the equatorial Pacific during the ensuing summer by inducing anomalous equatorial easterlies over the western-central Pacific^{22,48,49}, local air–sea interaction also jointly contributes to the anomalous anticyclonic circulation over the WNP. Simple AGCM simulations further examine the effects of these two drivers associated with IOD—IO “capacitor” warming and equatorial Pacific cooling—on summer circulations, clarifying that together these two significant SST forcings can induce an anomalous anticyclone with wider distribution in the meridional direction over the WNP.

In this study, we determine ENSO events based on the Niño 3.4 index without separating the different flavors. The Niño 3.4 region is where the SST is affected by both central Pacific (CP) and eastern Pacific (EP) ENSO, so the results reflect the combined influence of the different flavors of ENSO. Previous work has indeed suggested that different flavors of ENSO may have different modulating effects on IOD events^{25,52,53}: usually CP El Niño tends to have a relaxed relationship with the simultaneous positive IOD compared to EP El Niño (for example, in Table 2, the years of El Niño occurring without positive IOD all belong to CP El

Niño). This suggests that the internal variability of IOD (independent from ENSO) could be more significant in recent decades because ENSO itself may vary from the canonical EP type to more of the CP type.

The extreme wetness in eastern China in summer 2020 is found to be related to the preceding extreme positive IOD in 2019, drawing attention to this potentially significant delayed effect of IOD. Positive IOD can induce positive wind curl over the eastern SIO, which can consequently trigger Ekman downwelling and a westward-propagating oceanic downwelling Rossby wave; the downwelling Rossby wave reaches the southwestern IO around spring and leads to a warming SST anomaly, constituting the “capacitor” effect^{14,15}. However, how these processes work during other IOD events, and why the composite warming center differs from the 2019 IOD, is still unclear and warrants further investigation. Also, the present analysis analyzes mainly the aftermath of IOD in the ocean system and pays little attention to possible driving factors on land. Previous studies have also stated that snow cover over the continent may also help sustain the anomalous signals associated with IOD until the ensuing seasons^{35,36}; this possible intermediate effect of the land would also be interesting to investigate and compare in the future. Further clarification of the delayed effects of IOD and associated mechanisms on the ensuing summer precipitation in eastern China could provide a sounder basis for improving seasonal climate predictions with a longer lead time.

METHODS

Observational datasets

We downloaded the monthly precipitation data for the period of 1979–2021 from the Global Precipitation Climatology Project (GPCP) dataset published by NOAA/OAR/ESRL PSL, Boulder, CO, USA (<https://psl.noaa.gov/>), with a horizontal resolution of $2.5^\circ \times 2.5^\circ$ ⁵⁴. Station precipitation data are provided by the National Meteorological Information Center of China⁵⁵. The ERA5 reanalysis dataset of the same period archived at the European Centre for Medium-Range Weather Forecasts (ECMWF) is adopted, with a spatial resolution of $1^\circ \times 1^\circ$, and variables include geopotential height, vertical integral of water vapor flux, horizontal winds, vertical integral of water vapor flux divergence, sea surface pressure, and air temperature⁵⁶. Outgoing longwave radiation (OLR) with a resolution of $2.5^\circ \times 2.5^\circ$ is employed to demonstrate the atmospheric heat anomalies corresponding to IOD or ENSO, derived primarily from the high-resolution infrared radiation sounder (HIRS)^{57,58}. The SST fields in this study are represented by the monthly mean global Extended Reconstructed Sea Surface Temperature version 5 (ERSSTv5), with a horizontal resolution of $2^\circ \times 2^\circ$ ⁵⁹. Considering that SST over the tropical Indian Ocean has been increasing since 1950^{60,61}, the SST data are detrended prior to all analyses in this study.

Partial and composite analysis

In the current study, two indices are applied to represent the variation of IOD and ENSO events: the dipole mode index (DMI) during boreal autumn (September–November, SON), and the Niño 3.4 index during winter (December–February, DJF). The DMI represents the difference in SST anomalies between the western (10°S – 10°N , 50° – 70°E) and southeastern equatorial IO (10°S – 0° , 90° – 110°E)¹. The Niño 3.4 index is computed by averaging the SST anomalies over the Niño 3.4 region (5°S – 5°N , 170° – 120°W). Partial correlation analysis is conducted for seasonal fields with regard to the DMI/Niño 3.4 index to separate the influence of the other index by deducing the linear relation between them. To further investigate the different signals associated with different combinations of preceding IOD and ENSO forcing, composite analysis is employed in this study, with cases selected according to the intensity of the DMI and Niño 3.4 indices. Significance levels for the composite and partial correlation analyses are examined by the Student's *t*-test.

Model simulation

An anomalous atmospheric general circulation model (AGCM⁶²) is utilized to investigate the impacts of the important SST patterns associated with

IOD and ENSO on the ensuing summer precipitation. The model is developed based on the Princeton dynamic core⁶³ and consists of five sigma levels (0.1, 0.3, 0.5, 0.7, 0.9) with a horizontal resolution of T42. The anomalous AGCM can examine perturbations along with a given mean basic state (ideal or real). This model can be used to demonstrate atmospheric responses to prescribed heating^{51,64,65} as well as changes in time-scale variation^{66,67}. These applications prove its reliability for investigating the anomalous atmospheric responses associated with IOD and ENSO forcings.

DATA AVAILABILITY

The precipitation data from the GPCP and ERSSTv5 datasets are available at <https://psl.noaa.gov/>, and the ERA5 reanalysis data can be downloaded at <https://www.ecmwf.int/en/forecasts/datasets/reanalysis-datasets/era5>. The OLR dataset is accessible at <https://www.nccl.noaa.gov/products/climate-data-records/outgoing-longwave-radiation-monthly>.

CODE AVAILABILITY

The data in this study were processed and plotted by the NCAR Command Language (NCL). Codes used in this study are available upon request.

Received: 12 December 2021; Accepted: 13 May 2022;

Published online: 14 June 2022

REFERENCES

- Saji, N. H., Goswami, B. N., Vinayachandran, P. N. & Yamagata, T. A dipole mode in the tropical Indian Ocean. *Nature* **401**, 360–363 (1999).
- Webster, P. J., Moore, A., Loschnigg, J. P. & Leben, R. Coupled ocean–atmosphere dynamics in the Indian Ocean during 1997–98. *Nature* **401**, 356–360 (1999).
- Wu, B., Zhou, T. & Li, T. Seasonally evolving dominant interannual variability modes of East Asian climate. *J. Clim.* **22**, 2992–3005 (2009).
- Li, X. & Zhou, W. Quasi-4-yr coupling between El Niño–Southern Oscillation and water vapor transport over East Asia–WNP. *J. Clim.* **25**, 5879–5891 (2012).
- Chang, C. P., Zhang, Y. & Li, T. Interannual and interdecadal variations of the East Asian summer monsoon and tropical Pacific SSTs. Part I: Roles of the Subtropical Ridge. *J. Clim.* **13**, 4310–4325 (2000).
- Weng, H., Wu, G., Liu, Y., Behera, S. K. & Yamagata, T. Anomalous summer climate in China influenced by the tropical Indo-Pacific Oceans. *Clim. Dyn.* **36**, 769–782 (2011).
- Wang, B. et al. How accurately do coupled climate models predict the leading modes of Asian–Australian monsoon interannual variability? *Clim. Dyn.* **30**, 605–619 (2008).
- Lau, K. M. & Yang, S. Climatology and interannual variability of the Southeast Asian summer monsoon. *Adv. Atmos. Sci.* **14**, 141–162 (1997).
- Xie, S. et al. Indian Ocean Capacitor Effect on Indo-Western Pacific climate during the summer following El Niño. *J. Clim.* **22**, 730–747 (2009).
- Guan, Z., Ashok, K. & Yamagata, T. Summertime response of the tropical atmosphere to the Indian Ocean Dipole Sea Surface Temperature anomalies. *J. Meteorol. Soc. Jpn.* **81**, 533–561 (2003).
- Yang, J., Liu, Q. & Liu, Z. Linking observations of the Asian monsoon to the Indian Ocean SST: possible roles of Indian Ocean Basin mode and dipole mode. *J. Clim.* **23**, 5889–5902 (2010).
- Wu, R., Yang, S., Wen, Z., Huang, G. & Hu, K. Interdecadal change in the relationship of southern China summer rainfall with tropical Indo-Pacific SST. *Theor. Appl. Climatol.* **108**, 119–133 (2012).
- Qiu, Y., Cai, W., Guo, X. & Ng, B. The asymmetric influence of the positive and negative IOD events on China's rainfall. *Sci. Rep.* **4** <https://doi.org/10.1038/srep04943> (2014).
- Zhou, Z. Q., Xie, S. P. & Zhang, R. Historic Yangtze flooding of 2020 tied to extreme Indian Ocean conditions. *Proc. Natl Acad. Sci. USA* **118**, 1–7 (2021).
- Takaya, Y., Ishikawa, I., Kobayashi, C., Endo, H. & Ose, T. Enhanced Meiyu–Baiu rainfall in early Summer 2020: aftermath of the 2019 super IOD event. *Geophys. Res. Lett.* **47**. <https://doi.org/10.1029/2020GL090671> (2020).
- Zheng, J. & Wang, C. Influences of three oceans on record-breaking rainfall over the Yangtze River Valley in June 2020. *Sci. China Earth Sci.* **64**, 1607–1618 (2021).
- Li, H., Sun, B., Wang, H. & Yuan, X. Joint effects of three oceans on the 2020 super mei-yu. *Atmos. Ocean. Sci. Lett.* **15**, 100127. <https://doi.org/10.1016/j.aosl.2021.100127> (2022).
- Ding, Y., Liu, Y. & Hu, Z. Z. The record-breaking Mei-yu in 2020 and associated atmospheric circulation and tropical SST anomalies. *Adv. Atmos. Sci.* **38**, 1980–1993 (2021).
- Hendon, H. H. Indonesian rainfall variability: impacts of ENSO and local air–sea interaction. *J. Clim.* **16**, 1775–1790 (2003).
- Shinoda, T., Hendon, H. H. & Alexander, M. A. Surface and subsurface dipole variability in the Indian Ocean and its relation with ENSO. *Deep Sea Res. Part I Oceanogr. Res. Pap.* **51**, 619–635 (2004).
- Chen, H.-C. & Jin, F.-F. Fundamental behavior of ENSO phase locking. *J. Clim.* **33**, 1953–1968 (2020).
- Zhang, Y., Zhou, W. & Li, T. Impact of the Indian Ocean dipole on evolution of the subsequent ENSO: relative roles of dynamic and thermodynamic processes. *J. Clim.* **34**, 3591–3607 (2021).
- Alexander, M. A. et al. The Atmospheric Bridge: the influence of ENSO teleconnections on air–sea interaction over the Global Oceans. *J. Clim.* **15**, 2205–2231 (2002).
- Wang, B., Li, J. & He, Q. Variable and robust East Asian monsoon rainfall response to El Niño over the past 60 years (1957–2016). *Adv. Atmos. Sci.* **34**, 1235–1248 (2017).
- Zhang, W., Wang, Y., Jin, F.-F., Stuecker, M. F. & Turner, A. G. Impact of different El Niño types on the El Niño/IOD relationship. *Geophys. Res. Lett.* **42**, 8570–8576 (2015).
- Gualdi, S., Guilyardi, E., Navarra, A., Masina, S. & Delecluse, P. The interannual variability in the tropical Indian Ocean as simulated by a CGCM. *Clim. Dyn.* **20**, 567–582 (2003).
- Behera, S. K. et al. A CGCM study on the interaction between IOD and ENSO. *J. Clim.* **19**, 1688–1705 (2006).
- Yuan, Y., Zhou, W., Yang, H. & Li, C. Warming in the northwestern Indian Ocean associated with the El Niño event. *Adv. Atmos. Sci.* **25**, 246–252 (2008).
- Zhang, R., Sumi, A. & Kimoto, M. Impact of El Niño on the east Asian monsoon. *J. Meteorol. Soc. Jpn. Ser. II* **74**, 49–62 (1996).
- Huang, R. & Sun, F. Impacts of the Tropical Western Pacific on the East Asian Summer Monsoon. *J. Meteorol. Soc. Jpn. Ser. II* **70**, 243–256 (1992).
- Zhou, X. et al. Different responses of East Asian summer rainfall to El Niño decays. *Clim. Dyn.* **53**, 1497–1515 (2019).
- Lau, K. M. & Sheu, P. J. Annual cycle, quasi-biennial oscillation, and Southern Oscillation in global precipitation. *J. Geophys. Res.* **93**, 10975 (1988).
- Chang, C.-P., Harr, P. & Ju, J. Possible roles of Atlantic circulations on the weakening Indian Monsoon Rainfall–ENSO relationship. *J. Clim.* **14**, 2376–2380 (2001).
- Huang, R. & Wu, Y. The influence of ENSO on the summer climate change in China and its mechanism. *Adv. Atmos. Sci.* **6**, 21–32 (1989).
- Zhang, Y., Zhou, W., Chow, E. C. H. & Leung, M. Y. T. Delayed impacts of the IOD: cross-seasonal relationships between the IOD, Tibetan Plateau snow, and summer precipitation over the Yangtze–Huaihe River region. *Clim. Dyn.* **53**, 4077–4093 (2019).
- Kripalani, R. H., Oh, J. H. & Chaudhari, H. S. Delayed influence of the Indian Ocean dipole mode on the East Asia–West Pacific monsoon: possible mechanism. *Int. J. Climatol.* **30**, 197–209 (2010).
- Yuan, Y., Yang, H., Zhou, W. & Li, C. Influences of the Indian Ocean dipole on the Asian summer monsoon in the following year. *Int. J. Climatol.* **28**, 1849–1859 (2008).
- Huang, R., Chen, W., Yang, B. & Zhang, R. Recent advances in studies of the interaction between the East Asian winter and summer monsoons and ENSO cycle. *Adv. Atmos. Sci.* **21**, 407–424 (2004). 2004 213.
- Tanaka, M. Interannual and Interdecadal variations of the Western North Pacific Monsoon and Baiu Rainfall and their relationship to the ENSO cycles. *J. Meteorol. Soc. Jpn. Ser. II* **75**, 1109–1123 (1997).
- Ding, Y., Liang, P., Liu, Y. & Zhang, Y. Multiscale variability of Meiyu and its prediction: a new review. *J. Geophys. Res. Atmos.* **125**, e2019JD031496 (2020).
- Xie, S.-P. et al. Indo-western Pacific Ocean capacitor and coherent climate anomalies in post-ENSO summer: a review. *Adv. Atmos. Sci.* **33**, 411–432 (2016).
- Wu, R., Hu, Z. Z. & Kirtman, B. P. Evolution of ENSO-related rainfall anomalies in East Asia. *J. Clim.* **16**, 3742–3758 (2003).
- Wang, B., Wu, R. & Fu, X. Pacific–East Asian teleconnection: how does ENSO affect East Asian climate? *J. Clim.* **13**, 1517–1536 (2000).
- Luo, J. J. et al. Interaction between El Niño and extreme Indian Ocean dipole. *J. Clim.* **23**, 726–742 (2010).
- Liu, L., Yu, W. & Li, T. Dynamic and thermodynamic air–sea coupling associated with the Indian Ocean dipole diagnosed from 23 WCRP CMIP3 models. *J. Clim.* **24**, 4941–4958 (2011).
- Zhang, L., Han, W., Li, Y. & Shinoda, T. Mechanisms for generation and development of the Ningaloo Niño. *J. Clim.* **31**, 9239–9259 (2018).
- Gautier, C., Peterson, P. & Jones, C. Variability of air–sea interactions over the Indian Ocean derived from Satellite Observations. *J. Clim.* **11**, 1859–1873 (1998).

48. Izumo, T. et al. Influence of Indian Ocean Dipole and Pacific recharge on following year's El Niño: interdecadal robustness. *Clim. Dyn.* **42**, 291–310 (2014).
49. Izumo, T. et al. Influence of the state of the Indian Ocean Dipole on the following years El Niño. *Nat. Geosci.* **3**, 168–172 (2010).
50. Le, T., Ha, K. J., Bae, D. H. & Kim, S. H. Causal effects of Indian Ocean Dipole on El Niño–Southern Oscillation during 1950–2014 based on high-resolution models and reanalysis data. *Environ. Res. Lett.* **15**, 1040b6 (2020).
51. Wang, B., Wu, R. & Li, T. Atmosphere–warm ocean interaction and its impacts on Asian–Australian monsoon variation. *J. Clim.* **16**, 1195–1211 (2003).
52. Wang, X. & Wang, C. Different impacts of various El Niño events on the Indian Ocean Dipole. *Clim. Dyn.* **42**, 991–1005 (2014).
53. Yu, J. Y., Paek, H., Saltzman, E. S. & Lee, T. The early 1990s change in ENSO–PSA–SAM relationships and its impact on Southern Hemisphere climate. *J. Clim.* **28**, 9393–9408 (2015).
54. Adler, R. F. et al. The Version-2 Global Precipitation Climatology Project (GPCP) monthly precipitation analysis (1979–present). *J. Hydrometeorol.* **4**, 1147–1167 (2003).
55. Ren, Z., Yu, Y., Zou, F. & Xu, Y. Quality detection of surface historical basic meteorological data. *J. Appl. Meteorol. Sci.* **23**, 739–747 (2012).
56. Hersbach, H. et al. The ERA5 global reanalysis. *Q. J. R. Meteorol. Soc.* **146**, 1999–2049 (2020).
57. Lee, H.-T. et al. Development of the HIRS outgoing Longwave Radiation Climate Dataset. *J. Atmos. Ocean. Technol.* **24**, 2029–2047 (2007).
58. Lee, H.-T. NOAA CDR Program: NOAA Climate Data Record (CDR) of Monthly Outgoing Longwave Radiation (OLR), Version 2.7. NOAA National Centers for Environmental Information. <https://doi.org/10.7289/V5W37TKD> (2018).
59. Huang, B. et al. Extended Reconstructed Sea Surface Temperature, Version 5 (ERSSTv5): upgrades, validations, and intercomparisons. *J. Clim.* **30**, 8179–8205 (2017).
60. Du, Y. & Xie, S. P. Role of atmospheric adjustments in the tropical Indian Ocean warming during the 20th century in climate models. *Geophys. Res. Lett.* **35** <https://doi.org/10.1029/2008GL033631> (2008).
61. Alory, G., Wijffels, S. & Meyers, G. Observed temperature trends in the Indian Ocean over 1960–1999 and associated mechanisms. *Geophys. Res. Lett.* **34** <https://doi.org/10.1029/2006GL028044> (2007).
62. Li, T. Origin of the summertime Synoptic-Scale Wave Train in the Western North Pacific. *J. Atmos. Sci.* **63**, 1093–1102 (2006).
63. Held, I. M. & Suarez, M. J. A proposal for the intercomparison of the dynamical cores of atmospheric general circulation models. *Bull. Am. Meteorol. Soc.* **75**, 1825–1830 (1994).
64. Leung, M. Y. T., Cheung, H. H. N. & Zhou, W. Meridional displacement of the East Asian trough and its response to the ENSO forcing. *Clim. Dyn.* **48**, 335–352 (2017).
65. Zhang, Y., Zhou, W. & Leung, M. Y. T. Phase relationship between summer and winter monsoons over the South China Sea: Indian Ocean and ENSO forcing. *Clim. Dyn.* **52**, 5229–5248 (2019).
66. Jiang, X.-A. & Li, T. Reinitiation of the Boreal Summer Intraseasonal Oscillation in the Tropical Indian Ocean. *J. Clim.* **18**, 3777–3795 (2005).
67. Li, R. C. Y., Zhou, W. & Li, T. Influences of the Pacific–Japan Teleconnection Pattern on Synoptic-Scale Variability in the Western North Pacific. *J. Clim.* **27**, 140–154 (2014).

ACKNOWLEDGEMENTS

This work was jointly supported by National Natural Science Foundation of China Grants 42192563, 42005010, 42120104001, as well as the Hong Kong RGC General Research Fund 11306417. Jiepeng Chen was supported by the Independent Research Project Program of State Key Laboratory of Tropical Oceanography (LTOZZ2005).

AUTHOR CONTRIBUTIONS

Y.Z. and W.Z. initiated this study with input from all authors. X.W., W.Z., and Y.Z. analyzed and interpreted the results. S.C. and J.C. contributed to numerical implementation. S.L. provided support for data collection and calculation. Y.Z. and W.Z. drafted the manuscript with extensive contributions from X.W., S.C., J.C., and S.L.

COMPETING INTERESTS

The authors declare no competing interests.

ADDITIONAL INFORMATION

Supplementary information The online version contains supplementary material available at <https://doi.org/10.1038/s41612-022-00271-5>.

Correspondence and requests for materials should be addressed to Wen Zhou.

Reprints and permission information is available at <http://www.nature.com/reprints>

Publisher's note Springer Nature remains neutral with regard to jurisdictional claims in published maps and institutional affiliations.



Open Access This article is licensed under a Creative Commons Attribution 4.0 International License, which permits use, sharing, adaptation, distribution and reproduction in any medium or format, as long as you give appropriate credit to the original author(s) and the source, provide a link to the Creative Commons license, and indicate if changes were made. The images or other third party material in this article are included in the article's Creative Commons license, unless indicated otherwise in a credit line to the material. If material is not included in the article's Creative Commons license and your intended use is not permitted by statutory regulation or exceeds the permitted use, you will need to obtain permission directly from the copyright holder. To view a copy of this license, visit <http://creativecommons.org/licenses/by/4.0/>.

© The Author(s) 2022